Article:
Chen, Y., Lioudakis, E., Yang, T. et al. (2026) Mapping relaxation pathways and bottlenecks in 2D perovskite microcavities. Journal of Materials Chemistry C. ISSN: 2050-7526

https://doi.org/10.1039/d6tc01094f

Journal of Materials Chemistry C

ROYAL SOCIETY OF CHEMISTRY

PAPER

Published on 03 July 2026

Cite this: DOI: 10.1039/d6tc01094f

Mapping relaxation pathways and bottlenecks in 2D perovskite microcavities

Yan Chen,[a] Emmanouil Lioudakis,[b] Tingxiang Yang,[c] Timothy Thornber,[a] Alexandra J. Ramadan,[a] Andreas Othonos,[b] C. Neil Hunter,[c] Graham Leggett,[d] David G. Lidzey[a] and Kyriacos Georgiou *[b]

Received 6th April 2026,
Accepted 1st July 2026

DOI: 10.1039/d6tc01094f

rsc.li/materials-c

Exciton–polaritons in two-dimensional (2D) perovskites offer a promising platform for room-temperature polaritonics; however, their relaxation and scattering mechanisms remain only partially understood. Here, we report, for the first time, strong exciton–photon coupling in pure phase n = 1 butylammonium lead iodide (BA_2PbI_4) microcavities and employ femtosecond transient absorption (TA) spectroscopy to directly probe the underlying exciton-reservoir-to-polariton relaxation dynamics. Global analysis of the TA spectra reveals three distinct characteristic timescales: t_1 (< 1 ps), governed by ultrafast excitonic many-body interactions, including phase-space filling, Coulomb-screening, biexciton formation, and cavity-resonance reshaping; t_2 (5–15 ps), arising from exciton-reservoir-to-polariton scattering and exciton–exciton annihilation (EEA), together with bandgap renormalization (BGR); and t_3 (> 50 ps), associated with long-lived dark-state or trap-state relaxation. The decay-associated spectra (DAS) further indicate that although transient polariton-associated spectral response emerges on picosecond timescales, efficient population accumulation within the lower polariton branch (LPB) remains strongly limited by ultrashort polariton lifetimes, incomplete reservoir-to-LPB feeding, and nonradiative trapping processes. Taken together, these results provide a detailed ultrafast spectroscopic insight into the nonequilibrium relaxation pathways and kinetic bottlenecks governing 2D perovskite microcavities and offer guidance for future optimization strategies aimed at enabling room-temperature polariton condensation and nonlinear effects in pure phase n = 1 2D perovskite systems.

1. Introduction

Exciton–polaritons are hybrid light–matter quasi-particles formed *via* strong coupling between cavity photons and excitons, combining a low effective mass inherited from photons and a strong nonlinearity from excitons. These properties enable phenomena such as polariton lasing and Bose–Einstein condensation, positioning polaritonic systems as promising candidates for practical optoelectronic applications, particularly at elevated temperatures using organic semiconducting materials.[1–7] Two-dimensional (2D) lead halide perovskites, with their quantum-well-like inorganic $[PbI_6]^{4-}$ layers separated by organic cations (*e.g.*, *n*-butylammonium (BA^+), 2-phenethylammonium (PEA^+)), could also be considered as ideal materials for polaritonics. Their quantum confinement enhances exciton binding energies up to 200–400 meV,[8,9] stabilizing robust excitons at room temperature – a prerequisite for studying room temperature strong light–matter interactions. Recent reports have demonstrated a variety of nonlinear polariton effects in these materials, underscoring their potential for polariton lasers and quantum optoelectronic devices.[10–16] Despite these advances, achieving room-temperature polariton condensation in pure phase n = 1 2D perovskites remains elusive. In solution-processed perovskite microcavities, achieving a sufficiently high Q-factor remains a major challenge due to intrinsic material roughness, inhomogeneous broadening, and interfacial scattering losses.[17–19] To date, condensation has only been observed in exfoliated single crystals of n = 1 $(PEA)_2PbI_4$ at cryogenic temperatures.[20] In such phase pure systems, another important difficulty arises from an incomplete understanding of polariton relaxation dynamics, including how excitons scatter, thermalize, and populate the lower polariton branch (LPB). Non-radiative losses such as exciton–exciton annihilation (EEA), trap-assisted recombination, and exciton reservoir bottlenecks often dominate relaxation pathways, preventing the buildup of a sufficient population of polaritons in the ground state. In particular,

[a] School of Mathematical and Physical Sciences, The University of Sheffield, Hicks Building, Hounsfield Road, Sheffield S3 7RH, UK
[b] Laboratory of Ultrafast Science, Department of Physics, University of Cyprus, 1 Panepistimiou Avenue, 2109 Aglantzia, Nicosia, Cyprus. E-mail: georgiou.kyriacos@ucy.ac.cy
[c] School of Biosciences, The University of Sheffield, Alfred Denny Building, Sheffield S10 2TN, UK
[d] Department of Chemistry, The University of Sheffield, Brook Hill, Sheffield S3 7HF, UK

recent work on 2D $(PEA)_2PbI_4$ microcavities has further highlighted this inefficient radiative pumping of the LPB by multiple emissive channels within the exciton reservoir, thereby challenging polariton condensation.[21] However, this study primarily relies on steady-state and does not directly resolve the underlying ultrafast relaxation pathways.

Some other studies have begun to shed light on this complex picture. Liu *et al.* demonstrated that spin-dependent polariton–polariton interactions in 2D perovskite microcavities are highly sensitive to detuning and polarization, revealing strong many-body exchange processes that shape polariton scattering.[22] Fieramosca *et al.* identified that dark-state reservoirs and Coulomb-mediated interactions dominate the nonlinear response, emphasizing the role of non-emissive states in polariton decay.[23] Most recently, Fei *et al.* used ultrafast spectroscopy to demonstrate that strong light–matter coupling can suppress EEA by nearly an order of magnitude, as the photonic component of polaritons dilutes the exciton density and reduces scattering.[24] Together, these studies underline the complex interplay between bright polaritons, exciton reservoirs, and dark states, all of which govern energy relaxation and scattering in 2D perovskite systems. However, directly resolving polariton relaxation pathways remains challenging, particularly in ultrafast spectroscopy where overlapping excitonic and cavity-induced signals can obscure polariton contributions.[25]

In this work, we address this gap by employing femtosecond transient absorption (TA) spectroscopy to directly probe exciton–polariton relaxation in BA_2PbI_4 microcavities – a platform that has not been previously explored using ultrafast spectroscopy. While many demonstrations of perovskite polaritons rely on high-quality single crystals, our architecture represents a technologically relevant thin-film system in which disorder, grain boundaries, and nonradiative channels are inherently present. Importantly, the film quality achieved here is significantly improved compared to earlier thin-film studies,[19,26,27] as evidenced by the clear mode anti-crossing and well-defined polariton dispersion. This combination enables us to isolate intrinsic relaxation pathways in a realistic device geometry. By employing global lifetime analysis, we compare bare films and strongly coupled cavities with different detunings and identify distinct temporal regimes corresponding to carrier thermalization, exciton-to-polariton scattering, and long-lived dark-state dynamics. These results, therefore, provide direct spectroscopic evidence for energy transfer from the exciton reservoir to the LPB and reveal complementary time-resolved insight into the kinetic bottlenecks that hinder room-temperature polariton condensation in pure phase n = 1 2D perovskite microcavities.

2. Results

2.1 Strong coupling in BA_2PbI_4 microcavities at room temperature

The 2D perovskite semiconducting material that has been used in our experiments is n = 1 butylammonium lead iodide (BA_2PbI_4), synthesized with 4 mg ml^{-1} 18-crown-6 additive to provide additional crystallinity and uniformity (see SI, Fig. S2). The normalised absorption and photoluminescence (PL) spectra of a spin-coated non-cavity control film are plotted in Fig. 1a, with the BA_2PbI_4 crystal structure shown in the inset. A strong excitonic absorption feature is observed at ~510 nm with the corresponding PL spectrum having a narrow emission peak at 522 nm with a minimal Stokes shift (~12 nm). The small emission linewidth (17 nm full width at half-maximum, FWHM) that is evident here, reflects the strong excitonic character and the high degree of crystallinity of the perovskite film.

The microcavity structure fabricated was based on a spin-coated BA_2PbI_4 active layer, sandwiched between top and bottom dielectric Bragg reflector (DBR) mirrors (Fig. 1b). The DBRs were fabricated *via* electron-beam evaporation and consisted of 6 (bottom) and 4 (top) alternating $\lambda/4$-thick SiO_2 and TiO_2 layer pairs. The thickness of the alternate layers was carefully designed to allow for a DBR stopband centred at the wavelength of the perovskite's excitonic resonance (~510 nm) as shown in Fig. S1 of the SI. In the following paragraphs we focus on experiments undertaken on two different cavities that were characterised by a different exciton–photon detuning. To control cavity detuning, a poly(methyl methacrylate) (PMMA) layer was spin-coated on top of the perovskite, further stabilizing the architecture and acting as a spacer layer to directly adjust the cavity length. In the first cavity (P_{cav}), the photon mode was tuned to be at a higher energy as compared to the exciton energy (positively detuned cavity) while in the second cavity, the photon mode was negatively detuned with respect to the exciton energy (N_{cav}). Indeed, by tuning the thickness of the PMMA layer between 92 and 127 nm while keeping the perovskite thickness unchanged, we can directly modify the exciton–photon detuning, as demonstrated experimentally below.

Experimental angle-resolved white-light reflectivity from the microcavity samples shown in Fig. 1c and d, right panel, reveals clear anti-crossing behaviour between the cavity mode and the exciton resonance at room temperature, with the LPB wavelength at normal incidence being located at 521 nm (537 nm) in P_{cav} (N_{cav}). We have described this reflectivity dispersion using a transfer matrix method (TMM) model (see Fig. 1c and d, left panel), with good agreement between the model and measurement being obtained.

We have also modelled exciton–photon hybridization in the microcavities using a two-level coupled oscillator Hamiltonian that is summarised in eqn (1). The model was used to fit the energy of the polariton modes as identified in the angular dependent reflectivity spectra of Fig. 1c and d and is plotted using white dashed lines superimposed on the contour maps.

$$H = \begin{pmatrix} E_{cav}(\theta) & g \\ g & E_{ex} \end{pmatrix} \begin{pmatrix} C\pm \\ X\pm \end{pmatrix} \quad (1)$$

Here, $E_{cav}(\theta)$ is the cavity photon dispersion as a function of angle θ, E_{ex} is the peak exciton energy, and g is the exciton–photon coupling constant. Note that in this material system, the change in the peak exciton energy E_{ex} as a function of angle

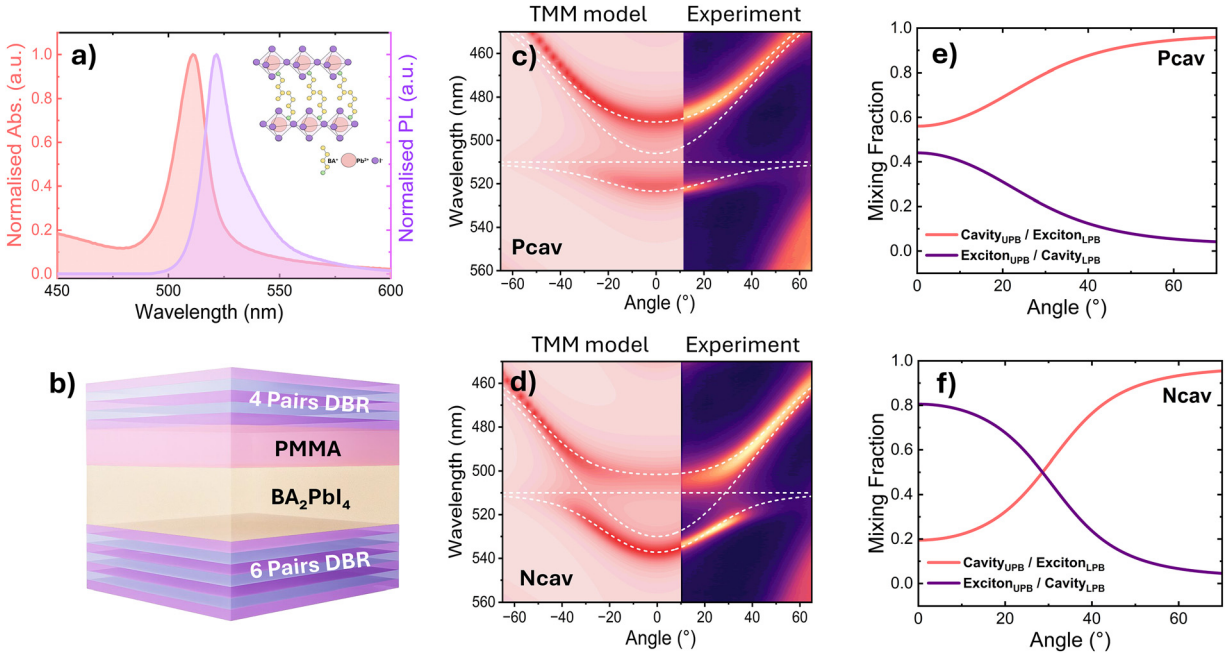

Fig. 1 (a) Normalised absorption and PL of an n = 1 BA_2PbI_4 film along with its crystal structure (inset); (b) schematic of the cavity structure; (c) and (d) simulation *vs.* experiment of angle-resolved reflectivity of the (c) positively detuned cavity (P_{cav}) and (d) negatively detuned cavity (N_{cav}), respectively. The left panels plot simulated data by a TMM model while the right panels represent experimental data. White dashed lines overlapped with the colormaps are the simulation results for the energy of cavity photon, exciton, and UPB/LPB extracted by a TMM and a coupled oscillator model. Hopfield coefficients of (e) P_{cav} and (f) N_{cav}.

is expected to be negligible if any, therefore we have used a fixed value of the peak absorption energy of the excitons of E_{ex} = 2.43 eV for the range of angles modelled. $C\pm$ and $X\pm$ are the angle-dependent photon and exciton mixing coefficients, respectively, of the upper (+) and lower (−) polaritons. Diagonalization of this Hamiltonian yields the energy of the upper (UPB) and lower (LPB) polariton branches. We can quantify cavity detuning D using $D = E_{cav} - E_{ex}$, where E_{ex} is the fixed peak absorption energy of the excitons and E_{cav} is the energy of the photon mode at normal incidence. From this, we calculate a detuning D for P_{cav} and N_{cav} giving a value of 20 and −100 meV, respectively.

Using eqn (1), we can also calculate the polariton eigenvectors corresponding to the Hopfield coefficients, which quantify the exciton and photon fractions of each polariton state:

$$|C \pm (\theta)|^2 = \frac{E_{cav}(\theta) - E \pm (\theta)}{E_{cav}(\theta) + E_{ex} - 2E \pm (\theta)} \quad (2)$$

$$|X \pm (\theta)|^2 = 1 - |C \pm (\theta)|^2 \quad (3)$$

with $|C \pm (\theta)|^2$ and $|X \pm (\theta)|^2$ being the photon and exciton weights as a function of angle, respectively, with $E \pm (\theta)$ being the angle-dependent energy of the UPB/LPB. These coefficients have been computed and indicated that in P_{cav} (see Fig. 1e) the LPB is more exciton-like with a fraction between 56% and 96% across all angles, while in N_{cav} (see Fig. 1f), the LPB has a smaller exciton fraction (19% at normal incidence). The UPB of P_{cav} has a dominant photonic character, having a photon fraction between 56% and 96%. In contrast, the UPB of N_{cav} is characterised by a greater excitonic weight compared to P_{cav} at normal incidence (81% compared to 44%). As we describe below, the difference between these two structures allows us to provide a microscopic explanation for the detuning-dependent relaxation pathways observed in the TA dynamics.

2.2 Polariton emission

We have explored polariton emission from a series of DBR microcavities containing PMMA/BA_2PbI_4 bilayers using both CW and pulsed non-resonant excitation. Note that although our study focuses primarily on P_{cav} and N_{cav}, we have also investigated PL from two additional negatively detuned cavities. The reason for this is that P_{cav} and N_{cav}, although ideal for TA measurements as the 6/4-pair DBR design offers reduced reflectivity and allows for stronger TA signals, suffer from relatively small Q-factors (∼80); a microcavity figure of merit that is important for polariton condensation. On the other hand, the two additional microcavities studied in PL (Fig. 2) are characterised by higher Q-factors due to the greater number of DBR pairs used (see details below), and therefore having higher chances to undergo polariton condensation. Typical emission data from BA_2PbI_4 microcavities are shown in Fig. 2 following low-power CW excitation at 405 nm (∼6.25 W m^{-2}); here, Fig. 2a shows a cavity having a Q-factor of ∼322 in which 6/8 DBR mirror pairs were placed either side of the active layer. Fig. 2b shows the emission from a slightly higher Q-factor (∼535) microcavity in which 8/12 DBR pairs surround the active layer. Here, the cavity Q-factor was determined from

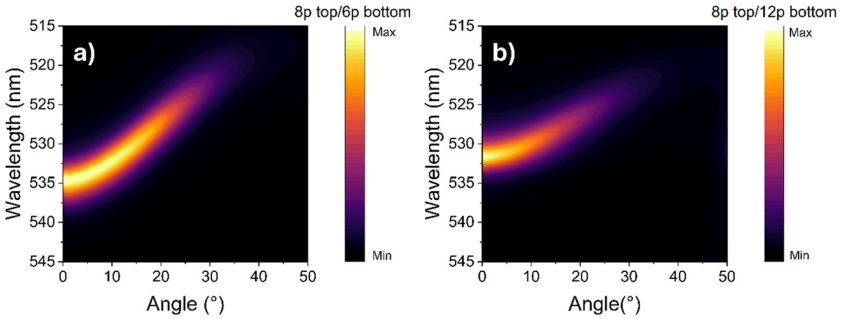

Fig. 2 Experimental angle-resolved PL spectra of (a) 6–8 pairs and (b) 8–12 pairs DBR negative-detuned cavities following 405 nm CW laser excitation.

the simulated normal-incidence cavity resonance according to $Q = \lambda_0/\Delta\lambda$. It can be seen that for both cavities, emission is distributed along the LPB, taking its maximum value around $\theta = 0^\circ$. We observe no evidence of emission from the UPB, indicating that there is rapid relaxation of any UPB polaritons to the exciton reservoir. The optical characterisation of the two additional cavities shown here can be found in Fig. S12 of the SI.

In order to explore whether cavities containing BA_2PbI_4 undergo polariton condensation, we have performed power-dependent femtosecond pulsed-excitation measurements on P_{cav}, N_{cav} and the two microcavities of Fig. 2, with measurements taking place at both room temperature and 4 K. However, across all excitation fluencies, the PL intensity increased linearly or sub-linearly with excitation power, providing no evidence of a threshold-like super-linear rise, linewidth collapse, or significant blueshift. With the absence of these hallmark signatures of polariton condensation, we have concluded that generating polariton lasing or non-linear effects in these structures are possibly hindered due to competing radiative and nonradiative loss channels that appear to deplete any polariton population build-up at the bottom of the LPB before the threshold can be reached.

2.3 Transient absorption and global fitting

To understand the processes that limit polariton relaxation and prevent polariton condensation, we have performed a detailed study on such structures using transient absorption (TA) spectroscopy, examining a range of time-windows, ranging from 1.3 ps before the arrival of the pump pulse to 500 ps after the pulse. The ultrafast TA measurements were carried out using a typical pump–probe optical setup in a non-collinear configuration (see SI, Section S5 for full details). Here, TA spectra were recorded following 400 nm non-resonant femtosecond excitation at two different pump fluences of 14 and 28 μJ cm^{-2}, with the pump beam incident at 5 degrees to the sample normal. This pump wavelength corresponds to a low reflectivity region of the DBR mirror (see Fig. S1) and is thus able to non-resonantly excite perovskite excitons. The supercontinuum white-light probe was then incident onto the cavity surface at normal incidence. This geometry gives access to the dynamics of polaritonic states near the bottom of the LPB dispersion ($\theta \approx 0^\circ$); states that are particularly relevant for evaluating reservoir-to-polariton feeding and population buildup associated with condensation.

We note that there are a number of different excitonic processes that lead to the types of spectral changes observed in TA signals, shown schematically in Fig. S9 of the SI. Phase-space filling (PSF) originates from the Pauli-exclusion principle; here states near the band edges become occupied by a high density of hot photocarriers. This pushes optical transitions to higher energies (causing a blueshift), which reduces the possibility of forming excitons (reducing effective oscillator strength[28]). Under strong coupling, this reduction in oscillator strength affects the exciton–photon coupling strength and therefore induces a partial Rabi-splitting energy contraction, leading to a transient blueshift of the LPB and a redshift of the UPB energies. Spectral blueshifts can also result from Coulomb screening. This occurs when there are many pump-induced free carriers that screen the Coulomb attraction between electrons and holes, thereby reducing the exciton binding energy (E_b).[29] As the exciton energy (E_x) can be described using $E_x = E_g - E_b$ (where E_g is the electronic bandgap), a reduced E_b effectively pushes the apparent excitonic edge to higher energies. Red shifts can result from the formation of biexciton states. These form when hot-excitons initially generated by the pump laser rapidly relax to the band edge. Such cooled excitons then bind, forming a biexciton with the energy of this state being smaller than the neutral exciton energy by a value associated with the biexciton binding energy.[30] Redshifts and broadening effects can also result from band-gap renormalisation (BGR). Here, BGR can variously result from many-body interactions between photo-excited carriers that reduce the E_g together with exciton–phonon coupling.[29]

We now discuss the spectral response of thin films and cavities following optical pumping. Representative $\Delta T/T$ spectra of the bare film and cavity samples at selected delays (top panels) along with their associated steady-state absorption spectra (bottom panels) are shown in Fig. 3a–c. In the control film (Fig. 3a), a prominent photobleaching (PB) feature appears near the exciton (510 nm), which is accompanied by derivative-like negative photoinduced absorption (PIA) sidebands around 484 and 527 nm. The resulting derivative-like spectral lineshape resembles that observed in other ultrafast studies of 2D perovskite systems, but the origin of these spectral features are still under debate.[31–34] In both P_{cav} and N_{cav} (Fig. 3b and c,

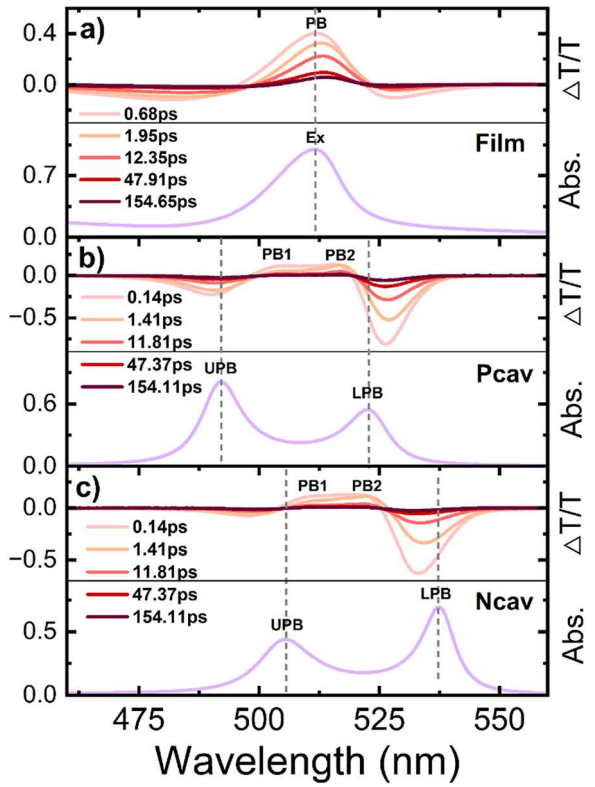

Fig. 3 TA ($\Delta T/T$) spectrum at different delay times under a 28 μJ cm^{-2} pump (upper panel) *vs.* steady-state absorption (bottom panel) of (a) a BA_2PbI_4 film, (b) P_{cav}, and (c) N_{cav}, respectively. Here, the steady-state film absorption has been experimentally measured while the absorption spectra of cavities are reproduced by our TMM model.

respectively), we observe two positive PB signals together with two negative derivative-like PIA sidebands. However, the two PB features do not correspond to the wavelength of the polariton branches but are instead located in the spectral region between the polariton branches.

To better understand the origin of the TA features and identify the factors that influence their energy and lineshape, we extract the linear optical transmission of a bare BA_2PbI_4 film at various pump–probe delay times $T_{pump\text{-}on}$ using the expression

$$\frac{\Delta T}{T} = \frac{T_{pump\text{-}on} - T_{pump\text{-}off}}{T_{pump\text{-}off}} \quad (4)$$

as shown in Fig. 4a. Here, $\Delta T/T$ values were taken from the experimental data, with the amplitude of the steady-state transmission $T_{pump\text{-}off}$ of the film being calculated using a TMM model based on the thickness of the sample layers used in the TA measurement. Note that the initial wavelength-dependent extinction coefficient parameters used as input for the TMM model are extracted from experimental transmission data of a bare BA_2PbI_4 film, with only the amplitude being adjusted by the model based on the film thickness. Here, our calculated spectra indicate that on photoexcitation, the film exhibits an instantaneous blueshift of 2 nm, moving from ~510 nm to ~508 nm (see the spectra shown in Fig. 4b), caused by a transient modification of the electronic band structure. This behaviour is primarily attributed to PSF and Coulomb screening. Following this, an energetic redshift then occurs, with the excitonic transition relaxing from ~508 nm to ~509 nm as delay time increases, (Fig. 4b). We mainly attribute this effect to BGR.[29,33,35]

Interestingly, we also find that a clear shoulder emerges at the low energy side of the main excitonic peak at early delay times (< 1 ps). We fit the transmission spectrum at 0.14 ps delay to three Lorentzian peaks at 488 nm, 508 nm, and 526 nm (see Fig. 4c). Here, a band at a higher energy of 488 nm having a linewidth of ~34 nm likely originates from optical transitions involving a continuum of unbound electron–hole pairs above the band edge (which we identify in the figure as "Con"). Apart from the exciton at 508 nm (marked "X"), we observe a shoulder at 526 nm that has previously been assigned to biexciton (marked "XX") formation.[36] We replot this fitted 526 nm peak at pump fluences of 14 and 28 μJ cm^{-2} in Fig. 4d. Here, the 526 nm feature shows a pronounced nonlinear increase in amplitude with increasing excitation density, consistent with the expected density-dependent behaviour of biexciton formation arising from exciton–exciton interactions. To further illustrate this behaviour, we have included the full experimentally extracted transmission spectra at this delay in Fig. S7 of the SI, normalised to the exciton (X) transmission minimum. This normalisation allows direct comparison of the relative biexciton contribution and reveals a significant increase in the amplitude of the biexciton-associated (XX) resonance relative to the exciton (X) feature at higher pump fluence, providing additional evidence for its biexcitonic origin. As the delay time increases beyond around 1 ps, the biexciton peak disappears and the transmission spectrum gradually recovers its equilibrium shape (Fig. 4a and b); a result consistent with carrier cooling, exciton recombination, and lattice relaxation processes that restore the band structure over a timescale of tens to hundreds of picoseconds.

We can use this approach in our TMM model to calculate the expected TA spectra of both cavities, attempting to reproduce the lineshape of the TA data. For this TMM-based spectral-shape modelling, we have selected the P_{cav} spectrum at 11 ps after excitation as a representative delay. At this time delay, the biexciton and continuum-band contributions that dominate the early-time response are substantially reduced, simplifying the spectral lineshape and enabling a more reliable analysis of the broadening and energy-shift effects. This choice was made solely to simplify the assignment of effects that influence the transient spectral lineshape.

Again, we include known underlying processes active in perovskite films; PSF (included *via* blueshifts and reduction in oscillator strength) and BGR (included *via* redshifts and a broadening of excitonic transitions). The effect of these processes on a transient absorption spectrum is shown schematically in Fig. S9. Here, it can be seen that both PSF and BGR result in the formation of a derivative lineshape due to their associated spectral shift, while the broadening associated with BGR also introduces further PIA features. We can use these basic ideas to examine the various processes that occur following photoexcitation of the control film and the cavity.

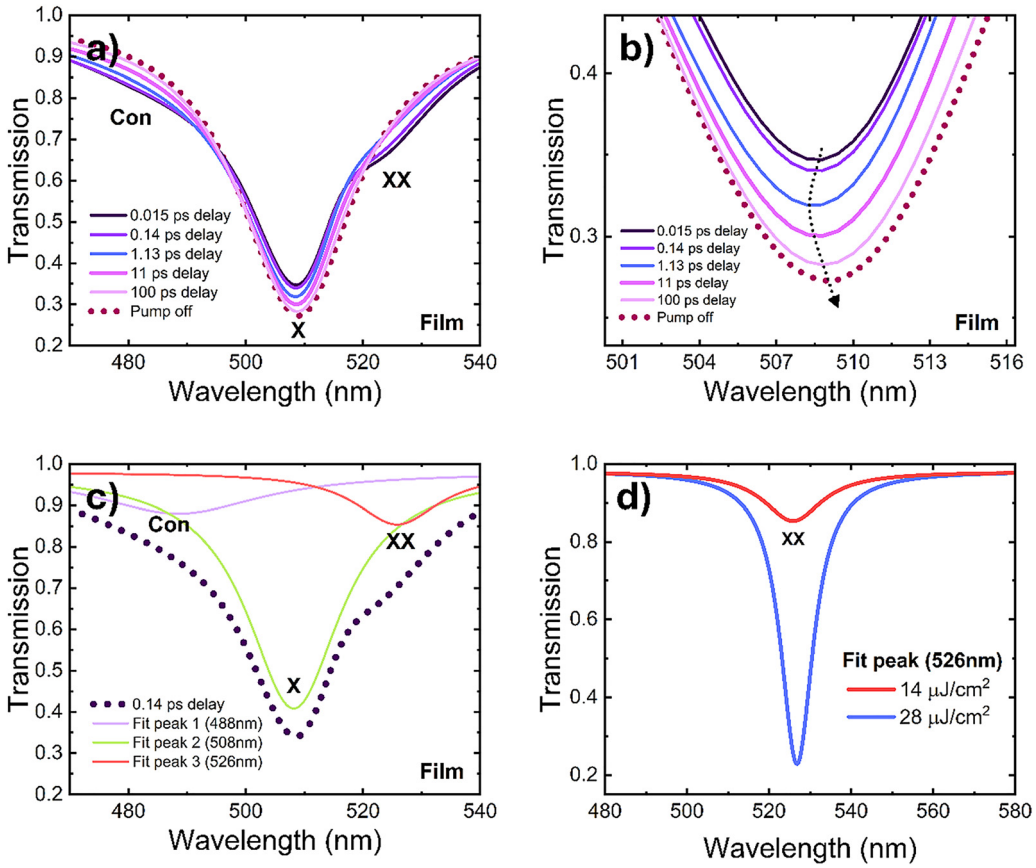

Fig. 4 (a) Transmission spectra of the film without a pump and following a 14 μJ cm^{-2} pump at different time delays. The dotted line is the transmission when the pump is off (as predicted using an experiment-informed TMM model). The coloured solid lines correspond to the measured transmission at different time delays as indicated in the inset. (b) Zoom-in on the exciton energy change shown in part (a), the black dashed arrow indicates the initial blueshift and the subsequent redshift; (c) the transmission spectrum following a 14 μJ cm^{-2} pump at 0.14 ps delay, with this fitted using 3 Lorentz peaks. (d) Shows the transmission spectrum of the feature at 526 nm extracted from a fitting to the transmission data at 0.14 ps delay. This fit is shown for a 14 μJ cm^{-2} and a 28 μJ cm^{-2} pump.

Fig. 5 plots the experimental differential transient transmission of P_{cav} at a delay of 11 ps following a 14 μJ cm^{-2} pump (black dashed line). We first apply a model in which the excitonic oscillator strength is reduced by 3%, corresponding to excitation-induced PSF that depletes the available excitonic states, as shown using an orange solid line. Our TMM calculations indicate that this 3% reduction in oscillator strength results in a Rabi splitting contraction from 287.2 meV to 282.9 meV. This suggests that excitation-induced oscillator-strength depletion contributes to the transient spectral shifts observed in the pump–probe signals. Here, we see a predicted region of PB around the energy of the UPB and LPB, and two side bands located at 486 and 528 nm. This simple model fails to adequately describe the measured data, as the strong bleaching predicted by the model around the UPB is not observed experimentally. We then explore a second model in which we apply a 0.5 nm blueshift to the exciton, combined with a relative broadening of 8% as shown using the blue line in Fig. 5. These values are obtained from the fitted data of the film transmission of pump-off and pump-on at a 11 ps delay, as shown in SI, Fig. S8. We believe this blueshift and broadening are caused by the combined effects of PSF and BGR; here, we note that at 11 ps, the exciton transmission is blueshifted with respect to its steady-state value (see Fig. 4b), although it is in fact redshifted compared to its value at much earlier times. This suggests that a number of effects are probably important here, including PSF and BGR. It is clear, however, that this model alone again fails to fully predict the experiment, as it results in a strong PIA at the UPB wavelength, with the wavelength of the LPB PB being relatively blueshifted by 9 nm.

To provide a better description of the data, we can in fact combine the two models (depletion, blueshift and broadening), with the prediction of the combined model shown using a dark solid line in the upper part of the plot. Here, the agreement between the model and experiment is improved (although clearly still not perfect); the model correctly predicts a small PIA corresponding to the UPB and a broad PB around the exciton energy and the LPB. We believe that the remaining discrepancies between this model and experiment likely arise from additional pump-induced effects, such as transient changes in the refractive index, layer thicknesses, and optical constants of the DBR, perovskite, and surrounding organic layers, with all of these effects driven through cavity-related spectral

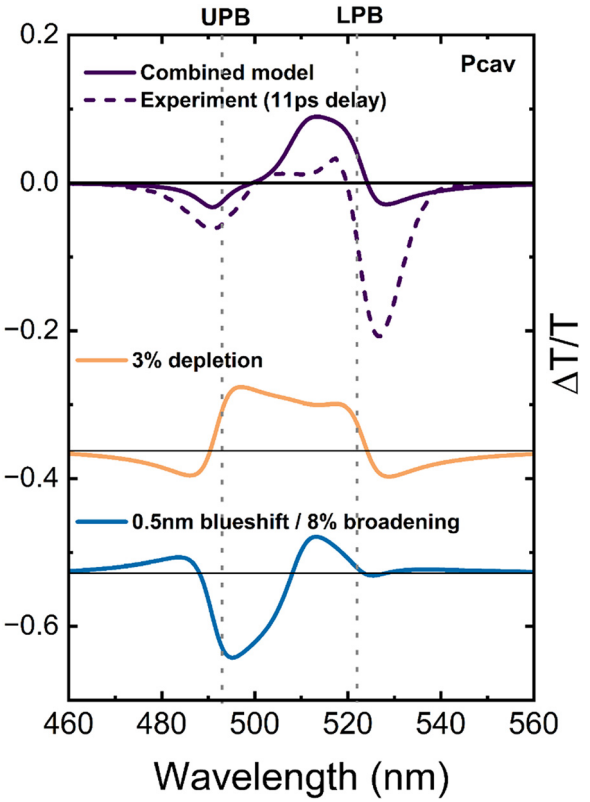

Fig. 5 Simulated *vs.* experimental $\Delta T/T$ spectra of P_{cav} under a 14 μJ cm^{-2} pump; solid line is the $\Delta T/T$ spectrum at a 11 ps delay and the dashed line is a simulation by our TMM model. The orange solid line in the bottom panel shows TMM simulation with 3% exciton depletion, the blue line represents a net result of BGR and PSF that broadens and blueshifts the exciton energy. Here, the depletion represents the decrease of amplitude of the oscillator caused by PSF.

distortions and thermal effects.[37] However, such pump-induced cavity artifacts are expected to be relatively weak compared to the strong exciton-related signals observed at early delay times. For this reason, these effects were not explicitly included in the model, which was intentionally simplified to isolate and reproduce the dominant contributions from PSF and BGR. The good qualitative agreement between the model and experiment indicates that PSF and BGR are the primary mechanisms governing the transient spectral reshaping, not only in the bare non-cavity films but also in the strongly coupled microcavities.

To further disentangle overlapping spectral contributions that influence the observed time-dependent features in the TA spectra, we performed a global lifetime analysis by simultaneously fitting the TA spectra across all wavelengths to a sum of exponentials convolved with the instrument response. Here, as shown in eqn (5), the TA data are fitted with a three-exponential decay function of the form:

$$y(t,\lambda) = A_1(\lambda)\times\exp\left(-\frac{t}{t_1}\right) + A_2(\lambda)\times\exp\left(-\frac{t}{t_2}\right) + A_3(\lambda)\times\exp\left(-\frac{t}{t_3}\right) + y_0 \quad (5)$$

where $A_i(\lambda)$ are the wavelength-dependent amplitudes, t_i are the fitted lifetimes shared across all probe wavelengths, and y_0 accounts for a long-time offset or a drift in the baseline. This shared-lifetime strategy allows us to extract global timescales of the system while simultaneously producing amplitude spectra that indicate which spectral regions are dominated by each of the different processes. The amplitude spectra $A_i(\lambda)$ extracted for each lifetime can then be analysed to assign spectral features. For example, we can associate PB at the exciton or LPB positions with an increase in exciton or polariton populations, while red- and blue-shifted PIA features indicate resonance reshaping induced by excitonic carrier populations. In this way, the global fitting decomposition can be used to directly link lifetime components to their corresponding spectral signatures in the TA data.

Using this approach, we can extract three characteristic lifetimes, t_1, t_2 and t_3, with each broadly associated with a distinct decay-associated spectrum (DAS). This is plotted in Fig. 6a–c, where the amplitude of the three different lifetime components for the control film and cavities as a function of wavelength is shown for the two different pump fluxes (14 and 28 μJ cm^{-2}). This analytical approach has been widely used in previous pump–probe research to study organic and perovskite system dynamics[38–41] as it allows a more robust assignment of dynamical processes to be achieved compared to single-wavelength fits. Further details about the employed global fitting method are provided in Section S7 of the SI.

It is worth noting that the estimated LPB lifetimes (τ_{LP}) are approximately 50 fs for the P_{cav} and 26 fs for the N_{cav} structures. These values are much shorter than the experimental temporal resolution determined by the ∼100 fs pump pulse duration. Therefore, the present transient absorption measurements are not expected to directly resolve the intrinsic LPB decay dynamics, and the observed sub-picosecond signals are instead attributed primarily to exciton reservoir relaxation and exciton-to-polariton scattering processes. Here, the LPB lifetime was estimated from the cavity photon lifetime (τ_{ph}) calculated using the expression $\tau_{ph} = \lambda_0 Q/2\pi c$. Assuming that the polariton decay is dominated by its photonic component, the LPB lifetime was approximated as $\tau_{LPB} \approx \tau_{ph}/|C|^2$.

2.3.1 Ultrafast time dynamics (t_1, 0.3–0.4 ps). The pink trace in Fig. 6a shows the DAS of the fastest component (t_1) in the non-cavity BA_2PbI_4 film, recorded at a pump flux of 14 and 28 μJ cm^{-2}, respectively. At 14 μJ cm^{-2}, we observe a pronounced PB centred at ∼507 nm, close to the 1s exciton resonance (∼510 nm, marked as E_x with a vertical dashed line), accompanied by derivative-like PIA sidebands at ∼480 nm and ∼525 nm. This spectral structure reflects several many-body processes that dominate immediately after photoexcitation. The strong PB arises primarily from PSF driven by hot-carrier thermalisation,[31] which reduces the exciton oscillator strength and thereby increases transmission at the exciton wavelength. We speculate that the derivative-like PIA sidebands result from a combination of the PSF/Coulomb screening-induced blueshift (producing the feature centred at ∼480 nm), with the feature at ∼525 nm resulting from BGR and formation of

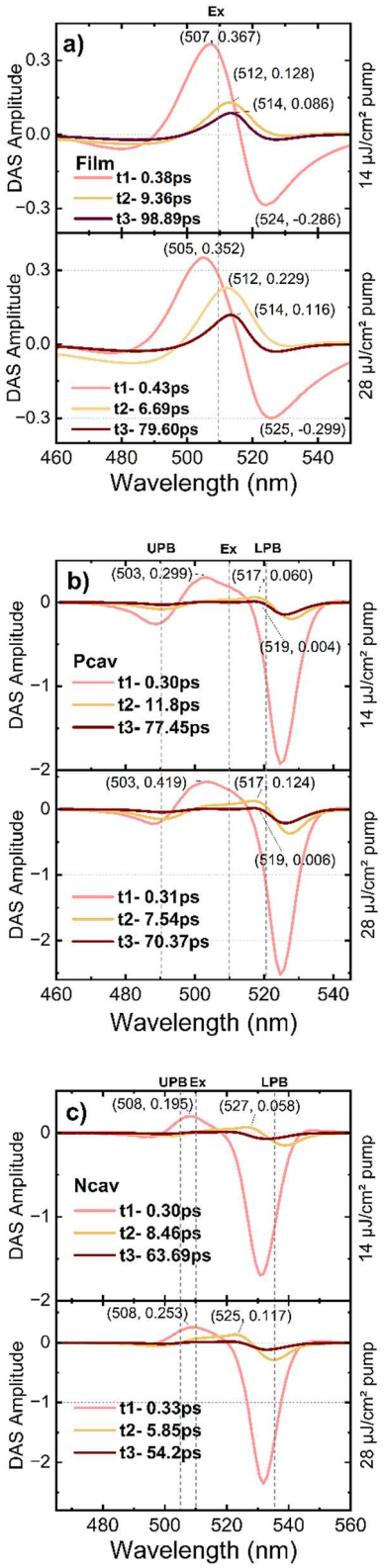

Fig. 6 Global fit of the TA spectra with the data presented recorded at two different pump fluxes: 14 and 28 μJ cm^{-2}. Data are shown for a (a) non-cavity film, (b) P_{cav} and (c) N_{cav}. In all cases, the pink-line corresponds to the fastest decay dynamics having t_1 = 0.3–0.4 ps, yellow corresponds to intermediate dynamics t_2 = 5–15 ps, with dark red representing the slowest dynamics t_3 = 60–100 ps. The vertical dashed lines correspond to the E_x, LPB and UPB wavelengths, respectively.

biexcitons.[42] At a higher pump flux (28 μJ cm^{-2}), the derivative-like lineshape remains, however, we find that the PB peak in the t_1 spectrum undergoes a 2 nm blue shift to 505 nm compared to the same peak recorded at a lower pump flux. This effect is consistent with carrier-dependent PSF and Coulomb screening effects, which drive a transient blue shift at early times, as discussed above.

Fig. 6b and c show the corresponding DAS of the t_1 component for P_{cav} and N_{cav} at both excitation fluences. In all cases, the spectra are dominated by a broad PB signal located between the UPB and exciton, a weak high-energy PIA at 485–495 nm caused by PSF/screening, and a stronger low-energy PIA band at 525–530 nm, which mainly results from BGR and the significant population of biexcitons that are formed at ultrafast times as discussed above. For convenience, we mark the peak of the UPB, E_x and LPB wavelengths as derived from steady-state reflection spectra using dashed lines. Here, bleaching signals around the condensation-relevant states within the LPB (in-plane momentum $k_{\parallel} \approx 0$) are absent during the ultrafast (<1 ps) regime. This indicates that a substantial population buildup at the bottom of the LPB dispersion is not observed within the current experimental temporal resolution. However, because the TA measurement geometry probes signals at normal incidence ($k_{\parallel} \approx 0$), we cannot exclude the possibility of ultrafast exciton-to-polariton scattering occurring at higher in-plane momenta (high-$k_{\parallel}$) outside the experimentally accessible angular window.

We also note that recent higher-time-resolution ultrafast spectroscopy studies on a different strongly coupled perovskite system [$(PEA)_2PbI_4$] have reported evidence of exciton-to-polariton scattering on sub-100 fs timescales.[43] In the present work, however, the combination of ~100 fs experimental temporal resolution and the strong excitonic many-body response dominated by PSF, Coulomb screening, biexciton formation, and early-stage BGR makes it difficult to isolate a distinct LPB-associated bleaching feature at low in-plane momenta (low-$k_{\parallel}$) during such earliest-time dynamics. Therefore, while ultrafast exciton-to-polariton scattering cannot be excluded in BA_2PbI_4 microcavities, particularly at finite $k_{\parallel}$, the dominant experimentally resolved response within the t_1 component is primarily dominated by excitonic effects (PSF, screening, early-stage BGR, and biexciton interactions), which strongly reshape the exciton resonance and the optical response of the polaritonic modes. The broad PB observed in t_1 therefore reflects a transient renormalised exciton resonance, together with its associated modulation of the polaritonic modes under non-resonant pumping. As we discuss below, a more pronounced transient response near the LPB energy emerges during the t_2 component, consistent with delayed reservoir-to-polariton feeding and population redistribution toward low-$k_{\parallel}$ LPB states on picosecond timescales.

Importantly, the two cavities show different high-energy PIA amplitudes. P_{cav} exhibits a pronounced blue-side PIA at ~489 nm near the UPB wavelength, whereas this feature is nearly absent in N_{cav}. This effect can be understood on the basis that the UPB in N_{cav} has a larger excitonic Hopfield fraction

than that in P_{cav} (56% *vs.* 19%). For this reason, we might expect that exciton-like UPB in N_{cav} to behave rather like an uncoupled exciton, undergoing a relatively large pump-induced exciton resonance reshaping, which results in a broader, more strongly damped optical mode that responds weakly to small excitonic perturbation. In other words, while the excitonic peak of the material itself experiences strong reshaping (PSF, screening, and broadening), this reshaping does not efficiently modulate the UPB when the mode is strongly exciton-like and heavily broadened. In contrast, the energy of the more photon-like UPB in P_{cav} is likely to be strongly affected by exciton-induced dielectric changes in the cavity refractive index, thermal heating, *etc.*, and will undergo a larger modulation of the UPB region in the TA spectrum.

This observation highlights that the transient spectral response of the strongly coupled cavities depends not only on the excitonic many-body interactions within the reservoir, but also on the optical sensitivity of the hybrid polaritonic modes to exciton-induced dielectric changes. Using a TMM model, we have simulated the transmission spectra of a series of cavities with different detunings resulting in polaritons with different photon–exciton mixing. By inducing a fixed excitonic perturbation in all detunings, we have simulated the associated TA spectra, showing that the blue-side PIA exhibits a non-monotonic dependence on the UPB photon fraction, peaking at intermediate mixing and diminishing for strongly exciton-like UPB states. This indicates that the PIA visibility is determined by an interplay between exciton-induced perturbations and the optical sensitivity of the cavity mode. Full details about our model together with the extracted results are discussed in Section S8 of the SI.

2.3.2 Intermediate time dynamics (t_2, 5–15 ps). The second kinetic component (t_2), shown as the yellow trace in Fig. 6, reveals pronounced differences between the bare BA_2PbI_4 film and the strongly coupled microcavities. In the control film (Fig. 6a), the DAS of t_2 peaks at 512 nm, close to the steady-state exciton absorption at 510 nm. This feature reflects exciton–exciton interactions, primarily BGR and EEA. The fluence dependence of the t_2 amplitude provides clear evidence for this; at higher excitation densities, the bleach amplitude increases while the lifetime shortens (Fig. 6a, bottom panel). This conclusion is consistent with EEA-induced depletion of exciton population and accelerated recombination dynamics.

In the strongly coupled cavities, however, the maximum of the t_2 DAS amplitude is redshifted relative to the film, appearing at 517 nm for P_{cav} and 527 nm for N_{cav} (Fig. 6b and c, respectively). These wavelengths approximately coincide with the LPB resonances, although the PB of the LPB is relatively blueshifted due (as we propose) to the carrier-induced PSF and BGR. The emergence of this LPB-associated bleaching feature on picosecond timescales suggests that the exciton reservoir increasingly feeds and modulates the low-$k_{\parallel}$ LPB states following the initial ultrafast carrier thermalization regime. Importantly, this picosecond response should not be interpreted as the lifetime of individual polariton states, since the LPB lifetime is estimated to be $\leq$50 fs from the cavity Q-factors. Instead, the data indicate a continuous dynamic process in which long-lived reservoir excitons scatter into and transiently populate low-$k_{\parallel}$ LPB states, with such polariton states rapidly decaying through photon leakage from the cavity. Because the reservoir-to-LPB feeding occurs on a timescale much slower than the LPB decay rate, efficient population accumulation at the bottom of the LPB dispersion is inhibited, resulting in a relaxation bottleneck that likely hinders polariton condensation under the present non-resonant excitation conditions.

A modest but measurable fluence-dependent enhancement in the t_2 bleaching amplitude is observed (from 0.06 to 0.124 in P_{cav} and from 0.058 to 0.117 in N_{cav}) along with a corresponding lifetime shortening, further confirming that EEA remains operative even under strong coupling. Notably, the P_{cav}, with its more exciton-like LPB, exhibits a slightly stronger t_2 bleach than the more photon-like N_{cav}, particularly at a higher excitation flux. This behaviour is consistent with previous reports showing that increasing the photonic fraction of a polariton mode dilutes its excitonic density, thereby reducing the strength of exciton–exciton interactions.[23]

It is also worth noting that the smaller LPB-associated bleach amplitude of t_2 as compared to the broad excitonic bleaching of t_1 suggests only a limited transient population buildup of the low-$k_{\parallel}$ LPB states. This observation may additionally reflect reverse scattering processes from low-$k_{\parallel}$ LPB states back into the exciton reservoir; a process that has previously been reported in strong-coupled organic polariton systems.[44] Collectively, these observations confirm that although the exciton reservoir dynamically feeds and modulates the LPB spectral response on picosecond timescales, competing annihilation, trapping, and bottleneck-limited relaxation processes likely suppress efficient low-$k_{\parallel}$ polariton accumulation required for condensation.

2.3.3 Long-lived time dynamics (t_3, 60–100 ps). The final decay component, t_3, dominates the late-time dynamics and is plotted in dark red in Fig. 6. In the non-cavity control-film (Fig. 6a), t_3 appears as a weak bleach slightly redshifted from the main exciton resonance (514 nm), consistent with the formation of lower energy long-lived dark- or trap-associated exciton states. In contrast, in both P_{cav} and N_{cav} (Fig. 6b and c), no distinct bleach is observed at either the exciton or polariton energies. Instead, a weak PIA feature emerges near the LPB region at 525–530 nm, suggesting that the residual population at long delays primarily resides in the dark or localized excitonic states that couple only weakly to the cavity field.

The absence of a pronounced LPB-associated bleaching signal at long delay times indicates that sustained feeding of low-$k_{\parallel}$ polaritonic states from the exciton reservoir becomes inefficient at long timescales. Instead, the weak red-side PIA observed in t_3 is consistent with nonradiative relaxation of excitons that have become localized through trapping states. Such localized excitons relax *via* phonon-assisted transitions from these bound states into higher vibronic manifolds, giving rise to a broad, low-energy absorption tail. Importantly, the low-energy PIA feature in t_3 is blueshifted relative to the corresponding PIA in t_2. This behaviour suggests that the strong

carrier-induced BGR present at earlier times has largely diminished due to carrier-density decay and reservoir depletion. Consequently, the transient modulation of the LPB optical response becomes significantly weaker at long delay times. Together, these observations indicate that the t_3 dynamics are dominated primarily by dark-state or trap-mediated exciton relaxation processes, rather than continued efficient reservoir feeding of low-$k_{\parallel}$ polaritonic states.

It is clear that there is a noticeable and general spectral blueshift of the t_1 trace compared to t_2 and t_3 that is evident in both the film and cavities. This originates from rapid PSF and Coulomb screening effects that occur immediately after photoexcitation as discussed earlier. High carrier densities partially occupy the band-edge states, reducing the exciton binding energy and thereby shifting the exciton resonance to higher energies, causing the observed blue shift. This blueshift may also be enhanced by a non-resonant photoexcitation-induced optical Stark effect (OSE).[34] As the carriers cool and PSF weakens, BGR becomes dominant, lowering the bandgap and shifting the exciton resonance to longer wavelengths causing a red shift, as reflected by the t_2 and t_3 bleaching features.

3. Discussion

We expect the efficiency of population transfer from the exciton reservoir to the LPB to be highly sensitive to the energetic overlap between the reservoir emission and the LPB minimum. When these are resonant, relaxation can proceed efficiently *via* emission–reabsorption processes, allowing polaritons to accumulate at the bottom of the dispersion.[45] To further evaluate this effect, we have compared the normalized PL spectra of the non-cavity BA_2PbI_4 film and PL measured at normal incidence from the two microcavity structures, as shown in Fig. S13 of the SI. Here, P_{cav} exhibits a slightly better spectral overlap between the exciton reservoir emission and the LPB emission at normal incidence as compared to N_{cav}. Here, the LPB/reservoir energetic overlap in conjunction with the photonic character of the polariton states is expected to determine the efficiency of the exciton-to-polariton scattering process into low-$k_{\parallel}$ LPB states.[46] In addition, the effective polariton lifetime at normal incidence estimated from the cavity Q-factor is slightly longer in P_{cav} ($\sim$ 50 fs) compared to that in N_{cav} ($\sim$ 26 fs), with this finding being consistent with the increased excitonic character of the LPB in the positively detuned cavity.

We believe that in the negatively detuned cavity studied, there is a polariton relaxation bottleneck that results in inefficient exciton-to-polariton scattering, preventing the effective establishment of a large polariton population at the LPB minimum. Such bottleneck behaviour is fully consistent with the TA dynamics discussed above. In both P_{cav} and N_{cav}, the t_2 component revealed an incomplete exciton-to-polariton transfer within a $\sim$10 ps timescale and a lack of sustained LPB population at longer time delays. Furthermore, the t_3 component is attributed to exciton trapping in long-lived dark or localized states, indicating the presence of residual nonradiative loss channels. Although the incorporation of the 18-crown-6 additive was found to improve film crystallinity, increase grain size, and reduce defect density compared with films prepared without additives, these trap states are not completely eliminated. In solution-processed BA_2PbI_4 thin films, disorder, grain boundaries, and interfacial defects can introduce localized states that compete with radiative feeding of the LPB.[33,47] Further improvements in crystal quality, particularly through the formation of larger grains and a reduction in grain-boundary density, together with enhanced defect passivation and optimisation of the perovskite/DBR interfaces, may help suppress nonradiative exciton trapping and increase the fraction of reservoir excitons available for exciton-to-polariton scattering.

Taken together, these results confirm that limited scattering efficiency, short polariton lifetimes, and strong nonradiative losses collectively prohibit the system from reaching the critical polariton density required for condensation under the conditions investigated. However, microcavity structures incorporating defect-control strategies, enhanced cavity Q-factors, and optimized detuning conditions could promote more efficient polariton population build-up, potentially enabling room-temperature condensation in pure-phase n = 1 2D perovskite microcavities.

Additionally, it is interesting to note that the negative derivative-like PIA sidebands observed in all three decay components originate from different microscopic mechanisms at each timescale. In the ultrafast regime ($<$1 ps), the PIA arises primarily from exciton phase-space filling, hot-carrier screening, and biexciton formation, which transiently reshape and blueshift the exciton resonance. During the intermediate t_2 dynamics, the PIA is dominated by LPB reshaping, where exciton-to-polariton scattering, BGR, and carrier-induced broadening jointly distort the LPB and exciton lineshapes. At late times (t_3), the remaining PIA feature originates mainly from trap-assisted or dark-state absorption, reflecting long-lived, nonradiative exciton populations that weakly perturb the optical response. The evolution of these PIA signatures thus captures the system's transition from coherent exciton–polariton dynamics at early delays to incoherent and defect-mediated relaxation as the system approaches equilibrium.

4. Conclusions

This work presents a comprehensive investigation of the ultrafast relaxation dynamics in strongly coupled pure phase n = 1 2D BA_2PbI_4 microcavities using femtosecond transient absorption spectroscopy. Global fitting analysis revealed a three-step relaxation sequence consisting of ultrafast carrier thermalization and exciton/biexciton formation (t_1), exciton-to-polariton scattering and exciton–exciton annihilation (t_2), and long-lived dark- or trap-state relaxation (t_3). A detailed spectral analysis indicates how these processes evolve under strong coupling and different detuning conditions.

Compared with the bare film, the microcavities exhibit a redshift of the t_2 bleaching feature from the exciton energy

toward the lower polariton branch, consistent with delayed reservoir feeding and population redistribution toward low-$k_{\parallel}$ LPB states on picosecond timescales. However, the absence of a clearly resolved sustained LPB-associated bleach at longer delay times, together with the ultrashort effective polariton lifetimes ($\leq$50 fs), indicates that efficient population accumulation at the bottom of the LPB dispersion is strongly limited under the present non-resonant excitation conditions. Instead, the transient response is dominated by the interplay between exciton reservoir relaxation, many-body excitonic interactions, cavity-induced spectral reshaping, and ultrafast modulation of the polaritonic modes. Furthermore, the observation of long-lived localized excitonic states implies that nonradiative trapping and disorder remain important kinetic bottlenecks in solution-processed BA_2PbI_4 microcavities.

Overall, this study provides direct ultrafast spectroscopic insight into the relaxation pathways in BA_2PbI_4 microcavities and highlights several factors, such as exciton–photon detuning, short polariton lifetimes, cavity losses, and the efficiency of exciton-reservoir-to-polariton transfer that likely influence polariton build-up under non-resonant excitation. These observations offer guidance for future optimization strategies aimed at improving polariton relaxation and potentially enabling the so-far elusive room-temperature condensation in pure phase n = 1 2D perovskite systems.

Author contributions

Y. C. designed and fabricated the cavities, performed the AFM measurements for the films, and carried out preliminary optical characterisation. E. L. and A. O. carried out the pump–probe measurements on films and cavities. Y. C. and T. Y. processed the pump–probe data and employed the global fit analysis. T. T. performed XRD for the films. A. R. provided perovskite synthesis expertise. Y. C., D. G. L., and K. G. wrote the manuscript with input from all the authors. K. G. provided overall supervision of the project.

Conflicts of interest

D. G. L. is a co-director of the company Ossila Ltd., which retails materials used in thin-film photonic research.

Data availability

The data supporting the findings of this study are available within the article and its supplementary information (SI). Supplementary information is available. See DOI: https://doi.org/10.1039/d6tc01094f.

Additional data that support the findings of this work are available from the corresponding author upon reasonable request.

Acknowledgements

K. G. acknowledges partial financial support from the European Union's Horizon Europe Research and Innovation Program under the Marie Skłodowska-Curie Grant Agreement No. 101066752 and from the Research and Innovation Foundation of Cyprus through the ''Bilateral Collaborations'' Programme (Cyprus RIF Grant Agreement No. ''BILATERAL/ISRAEL(MOST)/0224/0023'', SOLARITONICS). This work was partly funded by the Engineering and Physical Sciences Research Council (EPSRC) Programme Grant No. EP/T012455/1 (Molecular Photonic Breadboards), EP/M025330/1 (Hybrid Polaritonics), and EP/X039285/1 (Understanding the Electronic Structure Landscape in Wide Band Gap Metal Halide Perovskites).

References

1 T. Cookson, K. Georgiou, A. Zasedatelev, R. T. Grant, T. Virgili, M. Cavazzini, F. Galeotti, C. Clark, N. G. Berloff, D. G. Lidzey and P. G. Lagoudakis, *Adv. Opt. Mater.*, 2017, **5**, 1700203.
2 J. Keeling and S. Kéna-Cohen, *Annu. Rev. Phys. Chem.*, 2020, **71**, 435–459.
3 Z. Jiang, A. Ren, Y. Yan, J. Yao and Y. S. Zhao, *Adv. Mater.*, 2022, **34**, 2106095.
4 K. E. McGhee, A. Putintsev, R. Jayaprakash, K. Georgiou, M. E. O'Kane, R. C. Kilbride, E. J. Cassella, M. Cavazzini, D. A. Sannikov, P. G. Lagoudakis and D. G. Lidzey, *Sci. Rep.*, 2021, **11**, 1–12.
5 J. D. Plumhof, T. Stoeferle, L. Mai, U. Scherf and R. F. Mahrt, *Nat. Mater.*, 2014, **13**, 247–252.
6 K. S. Daskalakis, S. A. Maier and S. Kéna-Cohen, *Phys. Rev. Lett.*, 2015, **115**, 035301.
7 S. Kéna-cohen and S. R. Forrest, *Nat. Photonics*, 2010, **4**, 371–375.
8 K. Tanaka, T. Takahashi, T. Kondo, T. Umebayashi, K. Asai and K. Ema, *Phys. Rev. B:Condens. Matter Mater. Phys.*, 2005, **71**, 045312.
9 T. Ishihara, X. Hong, J. Ding and A. V. Nurmikko, *Surf. Sci.*, 1992, **267**, 323–326.
10 T. Wang, Z. Zang, Y. Gao, C. Lyu, P. Gu, Y. Yao, K. Peng, K. Watanabe, T. Taniguchi, X. Liu, Y. Gao, W. Bao and Y. Ye, *Nano Lett.*, 2022, **22**, 5175–5181.
11 R. Tao, K. Peng, L. Haeberlé, Q. Li, D. Jin, G. R. Fleming, S. Kéna-Cohen, X. Zhang and W. Bao, *Nat. Mater.*, 2022, **21**, 761–766.
12 I. Georgakilas, D. Tiede, D. Urbonas, R. Mirek, C. Bujalance, L. Caliò, V. Oddi, R. Tao, D. N. Dirin, G. Rainò, S. C. Boehme, J. F. Galisteo-López, R. F. Mahrt, M. V. Kovalenko, H. Miguez and T. Stöferle, *Nat. Commun.*, 2025, **16**, 5228.
13 R. Su, A. Fieramosca, Q. Zhang, H. S. Nguyen, E. Deleporte, Z. Chen, D. Sanvitto, T. C. H. Liew and Q. Xiong, *Nat. Mater.*, 2021, **20**, 1315–1324.
14 H. Chen, J. Lin, J. Kang, Q. Kong, D. Lu, J. Kang, M. Lai, L. N. Quan, Z. Lin, J. Jin, L. Wang, M. F. Toney and P. Yang, *Sci. Adv.*, 2020, **6**, eaay4045.

15 Y. Liang, Q. Shang, Q. Wei, L. Zhao, Z. Liu, J. Shi, Y. Zhong, J. Chen, Y. Gao, M. Li, X. Liu, G. Xing and Q. Zhang, *Adv. Mater.*, 2019, **31**, 1903030.
16 L. Lei, Q. Dong, K. Gundogdu and F. So, *Adv. Funct. Mater.*, 2021, **31**, 2010144.
17 G. Lanty, A. Bréhier, R. Parashkov, J. S. Lauret and E. Deleporte, *New J. Phys.*, 2008, **10**, 065007.
18 M. Laitz, A. E. K. Kaplan, J. Deschamps, U. Barotov, A. H. Proppe, I. García-Benito, A. Osherov, G. Grancini, D. W. DeQuilettes, K. A. Nelson, M. G. Bawendi and V. Bulovi, *Nat. Commun.*, 2023, **14**, 2426.
19 T. Fujita, Y. Sato, T. Kuitani and T. Ishihara, *Phys. Rev. B:Condens. Matter Mater. Phys.*, 1998, **57**, 428–434.
20 L. Polimeno, A. Fieramosca, G. Lerario, M. Cinquino, M. De Giorgi, D. Ballarini, F. Todisco, L. Dominici, V. Ardizzone, M. Pugliese, C. T. Prontera, V. Maiorano, G. Gigli, L. De Marco and D. Sanvitto, *Adv. Opt. Mater.*, 2020, **8**, 2000176.
21 M. Gomez-Dominguez, V. Quirós-Cordero, E. Rojas-Gatjens, K. A. Koch, E. J. Kumar, C. A. R. Perini, N. Stingelin, C. Silva-Acuña, A. R. Srimath Kandada, V. Menon and J. P. Correa-Baena, *ACS Photonics*, 2025, **12**, 2423–2431.
22 T.-Y. Liu, H. Wang, M.-S. Song, L.-Y. Zhao, Z.-F. Hu and H.-Y. Wang, *Laser Photonics Rev.*, 2022, **16**, 2200176.
23 A. Fieramosca, R. Mastria, K. Dini, L. Dominici, L. Polimeno, M. Pugliese, C. T. Prontera, L. De Marco, V. Maiorano, F. Todisco, D. Ballarini, M. De Giorgi, G. Gigli, T. C. H. Liew and D. Sanvitto, *Nano Lett.*, 2024, **24**, 8240–8247.
24 R. Fei, M. P. Hautzinger, A. H. Rose, Y. Dong, I. I. Smalyukh, M. C. Beard and J. van de Lagemaat, *J. Phys. Chem. Lett.*, 2024, **15**, 1748–1754.
25 S. Mukherjee, D. Bain, G. Davidova and A. Musser, *Nanophotonics*, 2026, **15**, e70049.
26 G. Lanty, S. Zhang, J. S. Lauret, E. Deleporte, P. Audebert, S. Bouchoule, X. Lafosse, J. Zuñiga-Pérez, F. Semond, D. Lagarde, F. Médard and J. Leymarie, *Phys. Rev. B:Condens. Matter Mater. Phys.*, 2011, **84**, 195449.
27 Y. Wei, J. S. Lauret, L. Galmiche, P. Audebert and E. Deleporte, *Opt. Express*, 2012, **20**, 10399–10405.
28 L. Wang, R. Nughays, J. Yin, C.-H. Shih, T.-F. Guo, O. F. Mohammed and M. Chergui, *ACS Photonics*, 2024, **11**, 2273–2281.
29 A. Chernikov, C. Ruppert, H. M. Hill, A. F. Rigosi and T. F. Heinz, *Nat. Photonics*, 2015, **9**, 466–471.
30 G. Yumoto, H. Tahara, T. Kawawaki, M. Saruyama, R. Sato, T. Teranishi and Y. Kanemitsu, *J. Phys. Chem. Lett.*, 2018, **9**, 2222–2228.
31 D. Babaian, D. Hill, Y. Ping and S. Guha, *J. Mater. Chem. C*, 2025, **13**, 193–202.
32 D. Giovanni, W. K. Chong, Y. Y. F. Liu, H. A. Dewi, T. Yin, Y. Lekina, Z. X. Shen, N. Mathews, C. K. Gan and T. C. Sum, *Adv. Sci.*, 2018, **5**, 1800664.
33 M. C. Gélvez-Rueda, S. Peeters, P.-C. Wang, K. M. Felter and F. C. Grozema, *Helv. Chim. Acta*, 2020, **103**, e2000121.
34 D. Giovanni, W. K. Chong, H. A. Dewi, K. Thirumal, I. Neogi, R. Ramesh, S. Mhaisalkar, N. Mathews and T. C. Sum, *Sci. Adv.*, 2016, **2**, e1600477.
35 Q. Li and T. Lian, *J. Phys. Chem. Lett.*, 2019, **10**, 566–573.
36 A. Shukla, G. Kaur, K. J. Babu, N. Ghorai, T. Goswami, A. Kaur and H. N. Ghosh, *J. Phys. Chem. Lett.*, 2020, **11**, 6344–6352.
37 S. Renken, R. Pandya, K. Georgiou, R. Jayaprakash, L. Gai, Z. Shen, D. G. Lidzey, A. Rao and A. J. Musser, *J. Chem. Phys.*, 2021, **155**, 154701.
38 N. P. Weingartz, M. W. Mara, S. Roy, J. Hong, A. Chakraborty, S. E. Brown-Xu, B. T. Phelan, F. N. Castellano and L. X. Chen, *J. Phys. Chem. A*, 2021, **125**, 8891–8898.
39 R. Malde, M. A. Parkes, M. Staniforth, J. M. Woolley, V. G. Stavros, V. Chudasama, H. H. Fielding and J. R. Baker, *Chem. Sci.*, 2022, **13**, 2909–2918.
40 W. Thor, H.-Y. Kai, Y.-H. Yeung, Y. Wu, T.-L. Cheung, L. K. B. Tam, Y. Zhang, L. J. Charbonnière, P. A. Tanner and K.-L. Wong, *JACS Au*, 2024, **4**, 3813–3822.
41 J. Xie, W. Zhou, H. Li, Z. Wang, J. Jiang, Y. Zhang, X. Shen, Z. Ning and W. Liu, *Adv. Opt. Mater.*, 2024, **12**, 2303004.
42 G. Kaur, K. Justice Babu, N. Ghorai, T. Goswami, S. Maiti and H. N. Ghosh, *J. Phys. Chem. Lett.*, 2019, **10**, 5302–5311.
43 V. Quirós-Cordero, E. Rojas-Gatjens, M. Gomez-Dominguez, H. Li, C. A. R. Perini, N. Stingelin, J. P. Correa-Baena, E. R. Bittner, A. R. S. Kandada and C. Silva-Acuña, *Phys. Rev. B*, 2026, **113**, L041102.
44 K. Georgiou, R. Jayaprakash, A. Askitopoulos, D. M. Coles, P. G. Lagoudakis and D. G. Lidzey, *ACS Photonics*, 2018, **5**, 4343–4351.
45 P. Deshmukh, S. Satapathy, E. Michail, A. H. Olsson, R. Bushati, R. K. Yadav, M. Khatoniar, J. Chen, G. John, B. W. Laursen, A. H. Flood, M. Y. Sfeir and V. M. Menon, *ACS Photonics*, 2024, **11**, 348–355.
46 R. T. Grant, P. Michetti, A. J. Musser, P. Gregoire, T. Virgili, E. Vella, M. Cavazzini, K. Georgiou, F. Galeotti, C. Clark, J. Clark, C. Silva and D. G. Lidzey, *Adv. Opt. Mater.*, 2016, **4**, 1615–1623.
47 W. Kaiser, K. Hussain, A. Singh, A. A. Alothman, D. Meggiolaro, A. Gagliardi, E. Mosconi and F. De Angelis, *J. Mater. Chem. A*, 2022, **10**, 24854–24865.

